4
Optics of White Blood Cells: Optical Models, Simulations, and Experiments

Valeri P. Maltsev, Alfons G. Hoekstra, and Maxim A. Yurkin

4.1
Introduction

4.1.1
White Blood Cells

The role of white blood cells (WBCs), or leukocytes, is to control various disease conditions and eliminate invading microorganisms. Although these cells do most of their work outside the circulatory system, they use the blood for transportation to sites of infection. Five types of white blood cells are normally found in the circulating blood: two mononuclear types (lymphocytes and monocytes) and three types of granulocytes (eosinophils, basophils, and neutrophils). Their presence relative to all leukocytes in normal conditions is in the ranges 18–44%, 2.6–8.5%, 46–73%, 0–4.4%, and 0.2–1.2%, respectively. And their characteristic size is 6–10 μm [1].

Lymphocytes and monocytes are cells with clear, transparent cytoplasm and large round nucleii. The lymphocytes mediate highly specific immunity against microorganisms and other sources of foreign macromolecules. B lymphocytes confer immunity through the production of specific, soluble antibodies, while T lymphocytes direct a large variety of immunity functions, including killing cells that bear foreign molecules on their surface membranes. Granulocytes and monocytes can exit from blood vessels and migrate among the cells of many tissues. These cells play key roles in inflammation and phagocytosis. Contrary to mononuclear cells, the nucleus of granulocytes is separated into definite lobes with a very narrow filament or strand connecting the lobes. Usually, two to three lobes are observed.

4.1.2
Particle Identification and Characterization

There exist two levels of scientific description of single particles in a disperse media: identification and characterization. Identification (also known as classification) means attributing the particles to one of several (usually predefined) classes, which

Advanced Optical Flow Cytometry: Methods and Disease Diagnoses, First Edition. Edited by Valery V. Tuchin.

can be distinguished from each other due to their morphological or/and functional characteristics. Characterization means quantitative measurement of a particle by its morphological and functional characteristics.

With reference to WBC analysis, identification corresponds to differential WBC count, that is, measuring the number (or fraction) of each of the five WBC types in the samples. This problem has been largely solved 20 years ago (Sections 4.1.3 and 4.3.2.1), using empirical methods based on vast experimental data. To develop the characterization method, one has to devise an optical model of the particle, and solve direct and inverse light-scattering problems.

Existing optical models of WBCs based on literature data and recently obtained-confocal images are described in Section 4.2. The methods used to simulate light scattering by optical models of WBCs range from the Mie theory to the discrete dipole approximation (DDA), and depend on the complexity of the model. Progress in the development of these methods and increase in computer literacy opened avenues for the development of new methods to solve the inverse light-scattering problem. In particular, it has become possible to perform an extensive search of the parameter space of a coated sphere model to perform fit of experimental light-scattering patterns of mononuclear WBCs. Both direct and inverse light-scattering problems for WBCs are discussed in Section 4.3.

4.1.3
Experimental Techniques

Light scattering and fluorescence offer a number of advantages in the identification and characterization of particles. For this purpose, various fluorescence-based and light-scattering methods have been used in scientific research and industries. Instrumentally, these methods can be divided into following categories: (i) methods based on analysis of light scattered by a particle suspension, and (ii) methods based on analysis of light scattered by individual particles. The first can be realized by using instruments measuring light scattering and fluorescence of particle ensembles. Today, however, the parameters of a distribution of particle characteristics can only be evaluated for very rough models of disperse media. Particle ensembles can be effectively studied using a single-particle analysis when light scattering and fluorescence are measured from individual particles with a sufficient rate for statistical data processing. In this case, determination of particle characteristics from light scattering is simplified substantially, whereas such instrumental approach requires solutions of technical problems that are related to fast detection of single particles. Fortunately, these problems were solved by flow cytometry, which utilizes hydrofocusing as a means for measuring scattering and fluorescent signals of individual particles.

Today, all large hospitals have facilities based on flow cytometry for detailed screening and identification of bacterial and blood cells of patients. Also, many research laboratories specialized in cell biology or immunology, all over the world, routinely apply cell identification and sorting to facilitate their research. A flow cytometer can identify single cells (at speeds as high as 50 000 cells/s) using elastic

light scattering from the cell, and fluorescence from fluorescent probes, which bind to specific molecules on the cell surface or inside the cell. Several fluorescence signals are measured, in combination with light-scattering signals. In this way, a number of independent measurements are obtained for every cell in the sample, and this information is used to identify different subsets in the original cell sample. However, at present, 95% of sorting facility of flow cytometers is based on an analysis of fluorescence, disregarding the advantages of light scattering for cell characterization.

During the last 15 years, researchers from the laboratory of Cytometry and Biokinetics, Institute of Chemical Kinetics and Combustion, Novosibirsk, Russia, have developed a revolutionary approach toward measuring light scattering in flow cytometry [2]. This scanning flow cytometer (SFC) allows detailed measurement of the entire angular light-scattering pattern (i.e., much more than in standard flow cytometry, in which light scattering is measured over only two different angles). The SFC offers exciting new ways to use flow cytometry, ranging from extending and improving routine measurements in hematology laboratories to applying it in new fields (such as microbiology).

Section 4.4 reviews application of the SFC to analysis of WBCs, including measuring absolute differential scattering cross section (DSCS) and characterization of lymphocytes from the measured light-scattering patterns.

4.2
Optical Models of White Blood Cells

4.2.1
Confocal Imaging of White Blood Cells

Confocal imaging of WBCs to construct optical models for light-scattering simulations was pioneered by Brock *et al.* [3] for cultured NALM-6 cells (a human B cell precursor). A Carl Zeiss LSM 510 META confocal microscope was used to develop optical models of lymphocytes and neutrophils. The parameters used for cell imaging are summarized in Table 4.1. The typical images of a lymphocyte and a neutrophil are shown in Figures 4.1 and 4.2, respectively.

4.2.2
Optical Models of Mononuclear Cells

The simplest model of mononuclear cells is a homogeneous sphere. It has been successfully used (explicitly or implicitly) to size lymphocytes using light-scattering signals by Neukammer *et al.* [4], Yang *et al.* [5], and Semyanov *et al.* [6]. To extract more morphological characteristics of mononuclear cells from experimental data, a more detailed model is required. Zharinov *et al.* [7] tested a multilayered sphere model, and showed that a five-layer model gave the best agreement between experimental and theoretical light-scattering profiles (LSPs).

Table 4.1 Parameters of the confocal microscopy.

Cell	Objective	Wavelengths (nm)	Filters (nm)	Scaling (nm)
Neutrophil	Plan-Apochromat 100 × /1.4 Oil DIC	405	BP 420–480	40 (x axis)
		488	505–530	40 (y axis)
		543	LP 560	310 (z axis)
Lymphocyte	Plan-Apochromat 100 × /1.4 Oil DIC	405	BP 560–615	20 (x axis)
		543	LP 420	20 (y axis)
		–	–	310 (z axis)

BP, bandpass; LP, landpass.

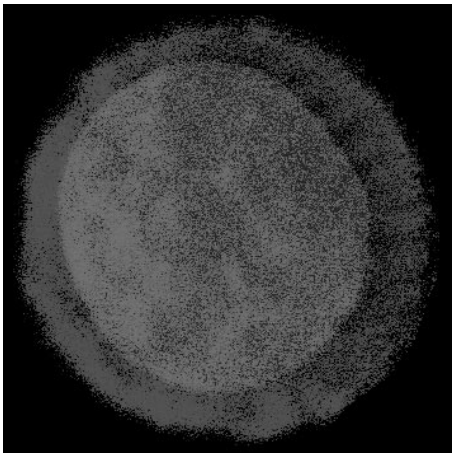

Figure 4.1 A slice from a confocal image of a lymphocyte.

However, this model is too complicated to provide reliable solution for the inverse light-scattering problems (Section 4.3.3), and its biological relevancy is not immediately clear.

For a simpler optical model, a more reliable procedure was recently proposed by Strokotov *et al.* [8]. From the confocal images (Figure 4.1), one can see that a coated sphere is an adequate first-order model, and this model has been used to solve the inverse light-scattering problem. However, it is also clear that the nucleus is certainly not perfectly homogeneous. To study the effect of such nuclear inhomogeneity on the light scattering, the optical model was enhanced by introducing an oblate spheroid into the nucleus. This model was used to mimic the effect that nuclear inhomogeneity may have on the LSPs and to verify the results of global optimization algorithms in the presence of model errors.

Another modification of coated sphere model was proposed by Hoekstra *et al.* [9] by shifting the nucleus from the cell center. Loiko *et al.* [10] proposed a

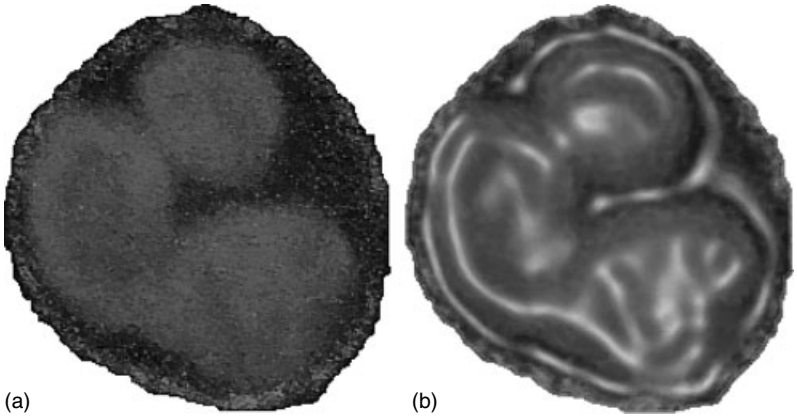

Figure 4.2 Slices from the confocal image of a neutrophil: original (a) and visually improved (b).

morphometric model of lymphocytes based on the images obtained by an optical microscope. This model consists of two nonconcentric spheroids and its main goal is to assist in the systematization of observational data. 3D models of precursor B cells have been constructed by Brock *et al.* [3] directly from confocal images. Unfortunately, such complicated models cannot be practically used to solve the inverse light-scattering problem.

4.2.3
Optical Models of Granular Cells

Granulocytes have the most complex morphology among all blood cells, featuring numerous granules and multilobed nucleus [1]. Although a simple homogeneous sphere model was used to determine the diameters of granulocytes [6], more detailed models are clearly required. Dunn [11] summarized two approaches to generate such models: (i) granules and nucleus (with certain random variations in size and shape) placed randomly inside the cytoplasm, and (ii) continuous random distribution of the refractive index within the cell or nucleus with certain spatial correlation lengths. In particular, Dunn [11] showed that both models produce LSPs, which were drastically different from that of homogeneous spheres, except for the forward-scattering direction.

A particulate model (i.e., of the type 1 above) of granulocytes was also used by Yurkin *et al.* [12]. It constitutes a sphere filled with identical spherical granules (Figure 4.3a) and its main goal was to study the influence of granules on LSPs. However, to match measured LSPs with simulations, a nucleus had to be included in the theoretical modeling. Orlova *et al.* [13] modeled a nucleus of neutrophils by four spheroids of various sizes, which were randomly placed and oriented inside the cytoplasm (Figure 4.3b). Geometrical parameters of this neutrophil model were based on literature data: the diameter of the cell $d_c = 9.6$ μm [6, 13]; granule

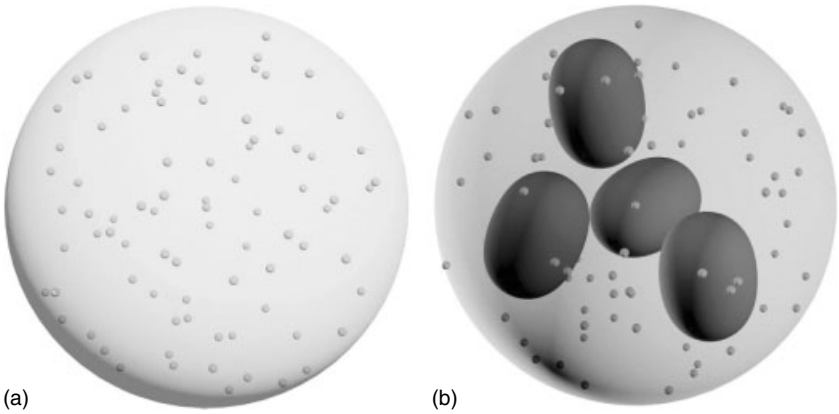

Figure 4.3 Optical models of (a) nuclei-free granulocyte and (b) neutrophil.

diameters $d_g = 0.1$, 0.15, and 0.2 μm [14, 15] and their volume fraction $f_g = 0.1$ [15, 16]; volume fraction of nuclei $f_n = 0.11$ [17, 18], resulting in total volume fraction of noncytoplasm material, granules and nucleus, equal to 0.2.

4.2.4
Refractive Indices of White Blood Cells and their Organelles

A necessary component of optical models is the refractive index of all its constituents. However, for WBCs, such data is hardly available in the literature. Dunn [11] collected information on refractive indices of the cell cytoplasm and constituents from several sources. However, none of them directly corresponds to human WBCs, while general ranges for cytoplasm and mitochondria are rather broad (1.35–1.38 and 1.40–1.42, respectively). Brunsting and Mullaney [19] reported a refractive index m_n of 1.39 for the nucleus of hamster ovary cells, which was used in simulations of granulocyte-type cells by Dunn [11].

Recently, refractive indices of mononuclear blood cells were determined by fitting LSP with five- or two-layer spherical models (Sections 4.3.3 and 4.4.4). Zharinov *et al.* [7] determined m_n of lymphocytes and monocytes in one sample to be 1.43 ± 0.05 (standard deviation, SD) and 1.43 ± 0.04, respectively. Strokotov *et al.* [8] studied samples of lymphocytes from seven donors and reported mean values between 1.44 and 1.45 with SD 0.01. Concerning the refractive index of cytoplasm m_c, Zharinov *et al.* [7] reported 1.356 ± 0.009 and 1.348 ± 0.004 for lymphocytes and monocytes, respectively. However, these results are arguable as they are based on the ambiguous correspondence between cytoplasm and the fourth layer of five-layer model. Strokotov *et al.* [8] reported significantly larger m_c: mean values between 1.376 and 1.377 with SD 0.003.

We are aware of only one other study where m_c of human lymphocytes was measured [20]. The index-matching method was used leading to mean value of m_c equal to 1.3572 ± 0.0002 (standard error of mean) for several normal donors,

which is lower than values obtained by Strokotov *et al.* [8]. This is because the latter determines the integral (effective) refractive index of the whole cytoplasm, including all granules and other inclusions, while index matching yields the value for the ground substance of the cytoplasm.

Brock *et al.* [3] used 1.3675 and 1.4 for m_c and m_n, respectively, for their B cell optical model. However, these values were taken from paper by Mourant *et al.* [21], who derived them from the study of light scattering by rat fibroblast cells.

It is almost impossible to choose reliable values for the refractive index of granulocyte granules m_g, because there seems to be no literature data available and there exist at least several different types of granules with different composition. Hence, the choice of any value of m_g to be used in light-scattering simulations is, to some extent, arbitrary. Yurkin *et al.* [12] varied the m_g from 1.47 to 1.6, the latter being close to the refractive index of dried protein [22]. Orlova *et al.* [13] chose intermediate refractive index 1.538 for both nuclei and granules to eliminate one free parameter of the model. Melanin with refractive index 1.7 was also used as granule material in optical models of cells [23, 24].

It is important to note that light-scattering patterns are sensitive to refractive index, and hence potentially this parameter can be determined with good accuracy from the solution of the inverse light-scattering problem (see above). However, the appropriateness of the used optical model has to be assumed. Moreover, we believe that all existing methods to determine refractive index of cell constituents are in some respect indirect: they either assume a certain optical model or measure some effective value (as index-matching technique). The ultimate goal is to develop a model-free method to solve inverse light-scattering problem, which, for example, computes the distribution of refractive index in the volume of the particle. But this goal is still far from reaching satisfactory accuracy [25].

4.3
Direct and Inverse Light-Scattering Problems for White Blood Cells

4.3.1
Simulation of Light Scattering by Mononuclear Cells

Spherical models of mononuclear cells are trivial with respect to light-scattering simulation. The theory of light scattering by single- or multilayered spheres is well known [26, 27] and LSPs are easily and quickly computed. To simulate light scattering by models lacking spherical symmetry, more general and slower methods have to be used. Methods based on surface discretization, such as extended boundary condition method [28] and null-field method with discrete sources [29], are especially effective for axisymmetric particles. Volume discretization methods, such as the DDA [30] and the finite difference time domain (FDTD, [31]) can handle any scatterers including inhomogeneous ones.

Hoekstra *et al.* [9] applied the DDA to a coated sphere model with shifted nucleus. It should be noted, however, that such a model can also be simulated

by a faster analytical algorithm [32]. Strokotov *et al.* [8] simulated light scattering by lymphocytes with inhomogeneous nucleus using the DDA. Brock *et al.* [3] and Ding *et al.* [33] used the FDTD to simulate light scattering by realistic 3D models of B cells precursors. Although both methods may now be used routinely for different cell models, the DDA has been proven to be more efficient than the FDTD for large biological cells (a factor of 10–100 faster with the same accuracy [34]).

4.3.2 Simulation of Light Scattering by Granular Cells

There were only a few studies that included simulation of light scattering by realistic models of granulocytes. The FDTD simulations of light scattering by a granulocyte-type model were performed by Dunn and coworkers (reviewed by Dunn [11]). Yurkin *et al.* [12] performed DDA simulations of light scattering by granulated sphere models, varying model parameters in the range of all granulocyte subtypes. Orlova *et al.* [13] simulated light scattering by a neutrophil model including four-lobed nucleus and compared it with experimental LSPs measured by an SFC. Below, we discuss the latter two papers in detail.

4.3.2.1 Granulocyte Model Without Nucleus

Yurkin *et al.* [12] employed a granulated sphere model for granulocytes (Figure 4.3a) with the goal to explain the difference in depolarization ratio between neutrophils and eosinophils reported by de Grooth *et al.* [35]. The default parameters of the model, based on literature data on morphology of granulocytes, were as follows: diameter of the cell $d_c = 8\,\mu m$, volume fraction of granules $f = 0.1$, $m_c = 1.357$, $m_g = 1.2$, $m_0 = 1.337$, $\lambda = 0.66\,\mu m$. The main variable was the granule diameter d_g, varying from 0.075 to $2\,\mu m$. Each DDA simulation was repeated 10 times for different random granule placements, resulting in mean value $\pm 2 \times$ SD for each simulated value. Additionally, the result for the limiting case of $d_g = 0$ was obtained by the Mie theory applied to a homogeneous sphere with a refractive index obtained by the Maxwell–Garnett effective medium theory [26].

Some of the model parameters varied from their default values; however, to limit the number of DDA simulations, each parameter was varied with others fixed. For each set of parameters, a whole range of d_g was calculated. Yurkin *et al.* [12] tried four additional values of f: 0.02, 0.05, 0.2, and 0.3; two values of d_c: 4 and $14\,\mu m$; two of m_g: 1.1 and 1.15; and one of m_c: 1; that is, no cytoplasm at all. All simulations were carried out using the ADDA computer code v. 0.76, which is capable of running on a cluster of computers parallelizing a single DDA computation [36].[1)]

The side-scattering signals were simulated exactly as described by de Grooth *et al.* [35]: total side-scattering intensity I_{SS}, total depolarized intensity $I_{\perp}$, and the depolarization ratio $D_{SS} = I_{\perp}/I_{SS}$. Aperture widths $\Delta\theta$ and $\Delta\phi$ were defined so

1) This code is freely available at *http://code.google.com/p/a-dda/*.

that scattering angles $\theta = 90^\circ \pm \Delta\theta$ and $\phi = 90^\circ \pm \Delta\phi$ are collected (the default values are $\Delta\theta = \Delta\phi = 25^\circ$). The experimental findings of de Grooth *et al.* [35] can be summarized as follows. The scatter plot of a sample containing eosinophils and neutrophils in $I_\perp$ versus I_{SS} coordinates shows a clear discrimination of two subtypes. The I_{SS} signals are almost the same, while $I_\perp$ are larger for eosinophils. Moreover, there is a significant correlation between $I_\perp$ and I_{SS} for both neutrophils and eosinophils. Discrimination between two subtypes is the most pronounced using D_{SS}, with mean values of 0.044 and 0.013 for eosinophils and neutrophils, respectively (averaged over a single sample). D_{SS} is almost constant when $\Delta\phi$ is decreased at fixed $\Delta\theta$ for both granulocyte subtypes.

The results of DDA simulations of side scattering by granulated spheres with the default set of parameters and varying granule diameter are shown in Figure 4.4. For each d_g, mean values of I_{SS} and $I_\perp$ and error bars corresponding to two SDs are shown. Labels near some of the points indicate the values of d_g. There are two ranges of d_g: from 0.1 to 0.25 μm and from 0.4 to 2 μm, corresponding to distinct regions. The range from 0.25 to 0.4 μm is intermediate, where I_{SS} and $I_\perp$ strongly, albeit differently, depend on d_g. The two regions in Figure 4.4 qualitatively correspond to the neutrophils and eosinophils on the plots by de Grooth *et al.* [35]. Considering the morphological characteristics of neutrophil and eosinophils granules, the difference in depolarized side scattering can be explained solely by the difference in d_g. Moreover, Yurkin *et al.* [12] showed that the qualitative two-region picture does not change when varying model parameters (as described above).

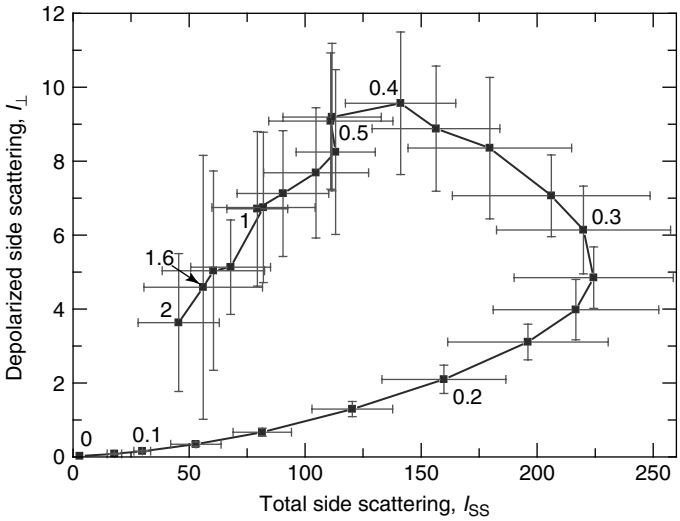

Figure 4.4 Depolarized versus total side-scattering intensities for several granule diameters from 0 to 2 μm, indicated for some points by labels, for the default set of parameters.

4.3.2.2 Approximate Theories

In addition to rigorous DDA simulations, Yurkin *et al.* [12] derived expressions for side-scattering signals based on approximate theories. The Rayleigh–Debye–Gans (RDG, [26]) approximation was used to calculate I_{SS}, and a two-order Born approximation (2-Born, e.g., [30]) was developed for $I_{\perp}$. Moreover, additional approximations were assumed during the derivation to obtain analytical expressions for values of I_{SS} and $I_{\perp}$, averaged over different granule placements. Accuracy of the theoretical expressions was assessed by comparison with DDA results for the default parameters of the granulated sphere model (Section 4.3.2.1). RDG results were calculated for three volume fractions $f = 0.02$, 0.05, and 0.1, while 2-Born was calculated only for the default one ($f = 0.1$). Yurkin *et al.* [12] concluded that the RDG is an accurate approximation for small f, especially for small x_g. However, it systematically underestimates I_{SS} for larger f owing to the ignored multiple scattering effects. The agreement between the 2-Born and the DDA is good, especially up to the first maximum. For larger x_g, the 2-Born approximation systematically underestimates the depolarized intensity, which is due to neglecting higher order scattering contributions and the fact that even a single large granule is treated inaccurately in the framework of the 2-Born approximation.

Although approximate theories are much faster than the DDA, their main added value consists in physical insight into the light-scattering problem, and the opportunity for an approximate solution for the inverse light-scattering problem. For instance, Yurkin *et al.* [12] derived the following scaling laws:

$$\langle I_{SS}\rangle \sim x_c^3 f \left|\frac{m_g - m_c}{m_0}\right|^2 \times \begin{cases} [1 + O(f)]x_g^3, x_g \ll 1 \\ O\left(x_g^{-1}\right), x_g \gg 1 \end{cases} \tag{4.1}$$

$$\langle I_{\perp}\rangle \sim x_c^3 f^2 \left|\frac{m_g - m_c}{m_0}\right|^4 \times \begin{cases} x_g^3[1 + O(f) + O(x_c x_g^3)], x_g \ll 1 \\ x_c O\left(x_g^{-2}\ln x_g\right), x_g \gg 1 \end{cases} \tag{4.2}$$

$$D_{SS} \sim f \left|\frac{m_g - m_c}{m_0}\right|^2 \times \begin{cases} 1 + O(f) + O\left(x_c x_g^3\right), x_g \ll 1 \\ x_c O\left(x_g^{-1}\ln x_g\right), x_g \gg 1 \end{cases} \tag{4.3}$$

where x_g and x_c are size parameters of granules and the whole cell, respectively. DDA simulations varying all model parameters (Section 4.3.2.1) showed that these scaling laws are more accurate, especially for D_{SS}, than approximate theories themselves.

4.3.2.3 Neutrophil Model with Nucleus

A limited set of light-scattering simulations for a neutrophil model with nucleus (Figure 4.3b) was performed by Orlova *et al.* [13], using ADDA v. 0.76 [36]. Geometrical parameters of the model are described in Section 4.2.3; a refractive index 1.357 was used for the cytoplasm, 1.458 for both the nuclei and the granules, and 1.337 for the outer medium. LSPs were evaluated in a form that corresponds to

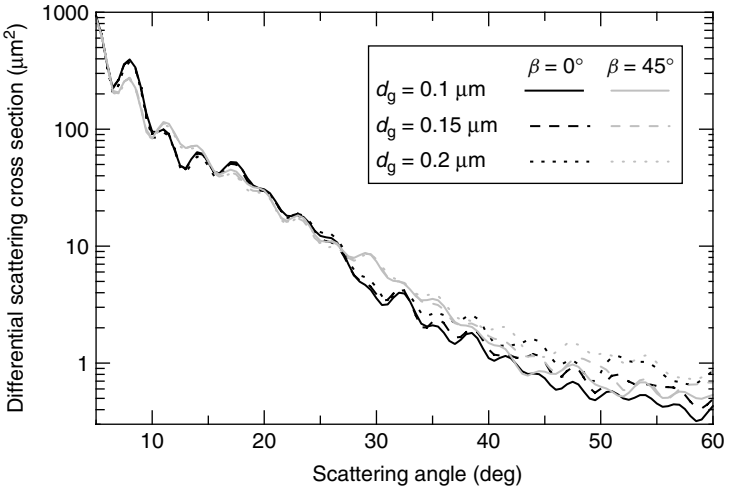

Figure 4.5 The LSPs calculated from DDA for the optical model of a neutrophil.

Eq. 4.17. Additional to varying d_g, two different orientations of the model with respect to the incident radiation were used (different by 45° rotation over Euler angle β). Six simulated LSPs are presented in Figure 4.5. They have different intensities for different granule sizes, but the differences are significant only for $\theta > 30°$, which agree with the results obtained by Yurkin *et al.* [12]. The overall adequacy of this optical model was proven by comparing it with experimental LSPs (Section 4.4.5).

4.3.3
Inverse Light-Scattering Problem for Mononuclear Cells

Unfortunately, the inverse light-scattering problem is much harder than the direct light-scattering problem. Previous studies, reviewed by Maltsev and Semyanov [2], concentrated on homogeneous spheres, prolate spheroids in a fixed orientation, and coated spheres (determining only the diameters). Recent advances include a spectral sizing method [37] – an empirical technique, whose applicability was demonstrated by extensive simulations for spheres [37], two-layer spheres [2], and erythrocytes [38]. This technique was applied to lymphocytes, monocytes, and granulocytes by Semyanov *et al.* [6] and produced meaningful results. Although the spectral method allows determination of refractive index of homogeneous spheres [37], it is at least hard to extend this property to a coated sphere and other models.

Zharinov *et al.* [7] proposed a solution for the inverse light-scattering problem for a five-layer spherical model of mononuclear blood cells, on the basis of an optimization procedure using multistart Levenberg–Marquardt algorithm. However, it has a few drawbacks. First, as the model has 10 free parameters (five radii

and five refractive indices for the corresponding layers), the search space is quite complex and it is hard to guarantee finding the global minimum. Although it was empirically proven that as many as 2500 restarts of the optimization procedure resulted in a reliable global minimum, such testing of robustness consumes a lot of computational time (about 1 h/cell). Second, and more importantly, that method did not provide (statistically reliable) errors of estimates of characteristics of individual cells, which is crucial to assess the overall adequacy of the fitting procedure.

Strokotov *et al.* [8] developed a solution for the inverse-light-scattering problem for mononuclear cells, modeled as a coated sphere. It is based on a global optimization technique and a new advanced statistical method to estimate errors of the deduced cellular characteristics. They also proposed a method to characterize the sample on the basis of individual measurements with varying errors. Below, we describe this approach in more detail.

4.3.3.1 Global Optimization

The solution for the inverse problem is performed by a least-square method, that is, by minimizing the weighted sum of squares:

$$S(\boldsymbol{\beta}) = \sum_{i=1}^{N} z_i^2,\ z_i = w(\theta_i)(I_{\text{th}}(\theta_i, \boldsymbol{\beta}) - I_{\exp}(\theta_i)) \tag{4.4}$$

where $\boldsymbol{\beta}$ is a vector of p model parameters, I_{th} and $I_{\exp}$ are theoretical and experimental LSP, respectively, $N = 160$ (in the range of θ from 12 to 50°), and $p = 4$ (described below). $w(\theta)$ is a weighting function given by

$$w(\theta) = \frac{1^\circ}{\theta} \exp\left(-2\ln^2(\theta/54^\circ)\right) \tag{4.5}$$

which goal is to reduce an effect of the noise on the fitting result [8].

To perform global minimization, DIRECT algorithm [39] is used, which performs an extensive search over the parameter space, described by a four-dimensional rectangular parallelepiped **B**, requiring a lot of computational time (a few minutes per lymphocyte). However, in addition to finding the global minimum of $S(\boldsymbol{\beta})$, that is, the best estimate $\boldsymbol{\beta}_0$, it provides an approximate description of the whole least-square surface, which we further use to estimate the parameter errors.

The following cellular characteristics are considered: cell diameter D_c, ratio of nucleus and cell diameters D_n/D_c, refractive indices of cytoplasm m_c, and nucleus m_n. For a particular case of human blood lymphocytes, the region **B** is defined by the following boundary values: $D_c \in [4.5, 10]$ μm, $D_n/D_c \in [0.7, 0.95]$, $m_c \in [1.34, 1.41]$, $m_n \in [1.41, 1.58]$.

4.3.3.2 Errors of Parameter Estimates

Most of the theories on nonlinear regression and errors of parameter estimates (see, e.g., Seber and Wild [40] and Bates and Watts [41]) are worked out for the case of normally distributed and independent experimental errors. Unfortunately, there

is significant dependence between residuals z_i in the case of lymphocytes, which can be characterized by a sample autocorrelation function ρ_k [40]. It is mainly caused by (i) model errors, that is, systematic difference between lymphocyte shape and a coated sphere, and (ii) imperfect alignment of SFC and noncentral position of the particle in the flow. Both types of these errors can be considered random for any particular lymphocyte.

Rigorous methods to deal with correlated residuals exist [40]; however, they are quite cumbersome. Strokotov *et al.* [8] proposed an approximate but much simpler approach, on the basis of the assumption that, for the purpose of statistical inference, N correlated residuals are equivalent to n independent residuals. The effective number of degrees of freedom n is determined by autocorrelation function

$$n = \frac{N^2}{N + 2\sum_{k=1}^{N-1}(N-k)\rho_k^2} \tag{4.6}$$

For lymphocytes that are studied, n is typically found to be from 10 to 25.

Next, a Bayesian inference method with standard noninformative (or homogeneous) prior $P(\sigma, \boldsymbol{\beta}) \sim \sigma^{-1}$ [40] is applied. The posterior probability density of $\boldsymbol{\beta}$ given a specific experimental LSP is then $P(\boldsymbol{\beta}|I_{\text{exp}}) = \kappa[S(\boldsymbol{\beta})]^{-n/2}$, where κ is a normalization constant obtained as

$$\kappa = \left(\int_{\mathbf{B}} \left[S(\boldsymbol{\beta})\right]^{-n/2} \mathrm{d}\boldsymbol{\beta}\right)^{-1} \tag{4.7}$$

To calculate integrals involving $[S(\boldsymbol{\beta})]^{-n/2}$ over $\mathbf{B}$, one can use the output of the DIRECT algorithm – a partition of $\mathbf{B}$ into $M(\sim 10^4)$ parts with volumes V_i and centers $\boldsymbol{\beta}_i$; with values $S_i = S(\boldsymbol{\beta}_i)$ also known. This is used to calculate an average of any quantity $f(\boldsymbol{\beta})$:

$$\langle f(\boldsymbol{\beta})\rangle = \kappa \int_{\mathbf{B}} f(\boldsymbol{\beta})\left[S(\boldsymbol{\beta})\right]^{-n/2} \mathrm{d}\boldsymbol{\beta} = \kappa \sum_{i=1}^{M} f(\boldsymbol{\beta}_i) S_i^{-n/2} V_i, \kappa = \left(\sum_{i=1}^{M} S_i^{-n/2} V_i\right)^{-1} \tag{4.8}$$

Knowing the complete probability distribution of model parameters for any measured particle, one can infer any statistical characteristics of this distribution, for example, the expectation value $\boldsymbol{\mu} = <\boldsymbol{\beta}>$ and the covariance matrix $\mathbf{C} = <(\boldsymbol{\beta} - \boldsymbol{\mu})(\boldsymbol{\beta} - \boldsymbol{\mu})^{\mathrm{T}}>$. Other quantities of interest are the highest posterior density (HPD) confidence regions, defined as $\mathbf{B}_{\text{HPD}}(P_0) = \{\boldsymbol{\beta}|P(\boldsymbol{\beta}|I_{\text{exp}}) > P_0\}$ [40]. Its confidence level is

$$\alpha = \kappa \int_{\mathbf{B}_{\text{HPD}}(P_0)} \left[S(\boldsymbol{\beta})\right]^{-n/2} \mathrm{d}\boldsymbol{\beta} \tag{4.9}$$

These confidence regions are used to assess the influence of parameter space boundaries on the results. Although $\mathbf{B}$ is quite large, its boundaries cut off tails of the distribution, causing bias in the determination of both $\boldsymbol{\mu}$ and $\mathbf{C}$. The bias increases with relative weight of the cut tail, so a confidence level α of the particle (more precisely, of associated probability distribution over $\boldsymbol{\beta}$) is defined as the

confidence level of the HPD region touching the boundary of **B**. The main purpose of α is to assess biases of $\boldsymbol{\mu}$ and **C**. Relative goodness of fit is better assessed by the matrix **C**.

4.3.3.3 Theoretical Tests Based on More Complicated Model

Since real lymphocytes can only approximately be described by a coated sphere, a characterization method can be tested by a virtual experiment using a more complicated model. First, one can shift the nucleus inside the coated sphere model. However, Strokotov *et al.* [8] reported that, when nucleus is relatively large ($D_n/D_c = 0.9$), the nucleus shift showed no considerable effect on the structure of the LSP, except for scattering angles larger than 40°. Such LSPs were successfully processed with the global optimization, resulting in a confidence level above 0.95 and an accurate estimation of the model parameters.

Second, the model including nucleus inhomogeneity (Figure 4.6) was tested. The following parameters for the initial coated sphere model were used: $D_c = 6.38$ μm, $D_n/D_c = 0.903$, $m_c = 1.3765$, average $m_n = 1.4476$. Dividing the nucleus into two domains, 1.3765 and 1.457 were chosen as the refractive indices for the inner spheroid and the rest of the nucleus, respectively. This was done to maximize the contrast and make the average (effective medium) refractive index of the nucleus equal to the one specified above. The spheroid had axis ratios 1 : 2 : 2, its volume was 0.108 of the whole nuclear volume, its center coincided with the center of the cell, the orientation of the symmetry axis with respect to the light incidence direction θ_0 was from 0 to 90° with a step of 30°. Results of processing the simulated LSPs with the global optimization are shown in Figure 4.7. The important conclusion is that the global optimization performed reliably on these distorted LSPs, that is, the real values of the initial model were well inside the confidence intervals (although the latter may be large).

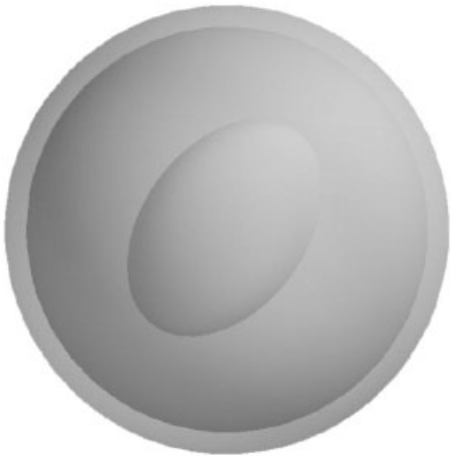

Figure 4.6 Optical model of a mononuclear cell with an inhomogeneous core.

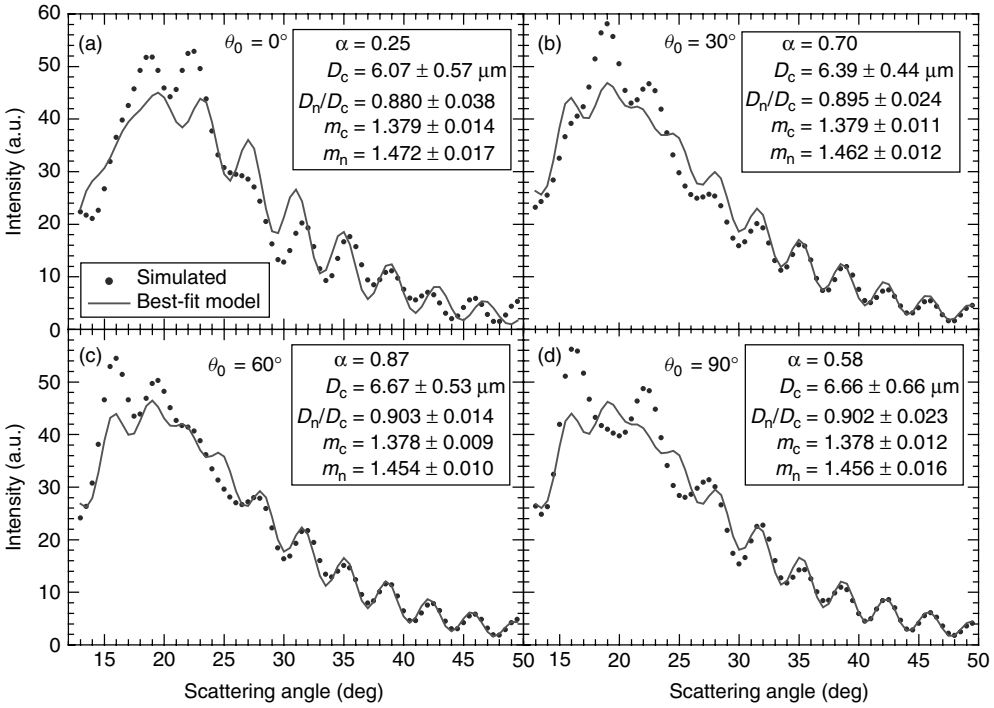

Figure 4.7 The LSPs calculated from DDA for the optical model of a lymphocyte with inhomogeneous nucleus.

4.3.3.4 Sample Characterization

Having determined the characteristics of each lymphocyte with certain errors (i.e., $\boldsymbol{\mu}_i$ and $\mathbf{C}_i$, $i = 1, \ldots, N_s$, N_s is the number of cells analyzed), Strokotov *et al.* [8] proposed the following method to estimate population mean and variances. General normal distributions are assumed for both the measurement results of individual particles and the true distribution of characteristics over a sample, the latter is described by a mean value $\mathbf{h}$ and covariance matrix $\mathbf{A}$. An estimator proposed by Fuller [42] is used, whose first step is based on the mean of $\boldsymbol{\mu}_i$ and $\mathbf{C}_i$ and a sample covariance matrix based on $\boldsymbol{\mu}_i$:

$$\overline{\boldsymbol{\mu}} = \frac{1}{n}\sum_i \boldsymbol{\mu}_i, \overline{\mathbf{C}} = \frac{1}{n}\sum_i \mathbf{C}_i, \overline{\mathbf{M}} = \frac{1}{n-1}\sum_i (\boldsymbol{\mu}_i - \overline{\boldsymbol{\mu}})(\boldsymbol{\mu}_i - \overline{\boldsymbol{\mu}})^{\mathrm{T}} \tag{4.10}$$

$\overline{\mathbf{M}} - \overline{\mathbf{C}}$ is an unbiased estimator of $\mathbf{A}$, but it should be modified to ensure positive semidefiniteness: $\mathbf{A}^{(0)} = \mathbf{F}(\overline{\mathbf{M}}, \overline{\mathbf{C}})$, where the transformation $\mathbf{F}$ is defined as

$$\mathbf{F}(\mathbf{X}, \mathbf{Y}) = \mathbf{X}^{1/2}\mathbf{Q}\mathbf{D}'\mathbf{Q}^{\mathrm{T}}\mathbf{X}^{1/2}, \text{where } \mathbf{I} - \mathbf{X}^{-1/2}\mathbf{Y}\mathbf{X}^{-1/2} = \mathbf{Q}\mathbf{D}\mathbf{Q}^{\mathrm{T}}, \mathbf{D}' = \max(0, \mathbf{D}) \tag{4.11}$$

The second step is the following:

$$\mathbf{X}_i = \left(\frac{n-1}{n}\left(\mathbf{A}^{(0)} + \mathbf{C}_i\right) + \frac{1}{n}\overline{\mathbf{M}}\right)^{-1}, \mathbf{Z} = \left(\sum_i \mathbf{X}_i\right)^{-1}, \boldsymbol{\mu}_0 = \mathbf{Z}\sum_i \mathbf{X}_i\boldsymbol{\mu}_i$$
$$\mathbf{M}_0 = \mathbf{G}\left(\left\{\mathbf{X}_i, (\boldsymbol{\mu}_i - \boldsymbol{\mu}_0)(\boldsymbol{\mu}_i - \boldsymbol{\mu}_0)^{\mathrm{T}}\right\}\right), \mathbf{C}_0 = \mathbf{G}\left(\{\mathbf{X}_i, \mathbf{C}_i\}\right), \mathbf{A}^{(1)} = \mathbf{F}(\mathbf{M}_0, \mathbf{C}_0) \tag{4.12}$$

where $\mathbf{G}(\{\mathbf{X}_i, \mathbf{Y}_i\})$ is a solution of the matrix equation

$$\sum_i \mathbf{X}_i\left(\mathbf{Y}_i - \mathbf{G}\right)\mathbf{X}_i = 0 \tag{4.13}$$

Equation 4.12 is iterated to convergence. The resulting $\boldsymbol{\mu}_0$ is an estimate for $\mathbf{h}$, whose covariance matrix (error of mean) is $\mathbf{Z}$ [42], and $\mathbf{A}^{(k)}$ is an estimate of $\mathbf{A}$.

The advantage of this procedure is that measurements which show large errors become insignificant. Therefore, one can seamlessly include all measurements into the estimation of cell characteristics, even those that seem unreliable due to large sum of squares and/or SDs of the characteristics. However, doing so is not the best option because of the bias due to the region boundaries, which are especially important for particles with small confidence level α. Therefore, only particles with $\alpha \geq \alpha_0$ are considered for characterization of the samples. Strokotov *et al.* [8] showed that $\alpha_0 = 0.8$ is a logical compromise between large number of processed cells (required to decrease error of mean) and smallness of systematic bias. Moreover, the moderate variation of α_0 does not significantly change the results.

It is important to note that the proposed method allows one to estimate a full covariance matrix of the sample of individual lymphocytes as well, including correlations between different characteristics. In Section 4.4.4, we show and analyze only the diagonal elements of the matrices $\mathbf{A}$ and $\mathbf{Z}$, that is, variances of the characteristics over the sample and errors of mean values. However, correlations are significant, for example, the correlation between D_c and both m_c and m_n are generally between -0.6 and -0.8, which is an interesting topic for future study.

We also emphasize that the method described in this section, which was originally developed for lymphocytes by Strokotov *et al.* [8], can be easily adapted to any biological cell modeled by a concentric coated sphere, including monocytes and stem cells.

4.4
Experimental Measurement of Light Scattering by White Blood Cells

4.4.1
Scanning Flow Cytometer

SFC is an instrument designed to measure the angular LSP of an individual particle [43–46]. The LSP is measured by guiding a particle or a cell through the measurement cuvette of the SFC and illuminating it with laser light. At present, the

SFC allows measurement of LSPs of individual cells with a rate of 500 particles/s within the measurable range of scattering angles ranging from 5 to 100°. The basic principle of the SFC was patented [47].

Combining the SFC with a solution of the inverse light-scattering problem potentially allows characterization of individual particles from light scattering with a typical rate of a few hundred particles per second. Characterization means determination of the physical particle characteristics such as size, shape, density, and so on. This is made possible by information contained in the measured LSP contrary to the ordinary flow cytometry, in which only the forward- and side-scattering signals are used.

4.4.1.1 The Current State of the Art of the SFC

The current state of the art of SFC technology relates to the instrumental platform of the universal analyzer for biology and medicine BioUniScan™ (CytoNova Ltd., Novosibirsk, Russian Federation). The core of the BioUniScan is formed by an SFC joining the optical and hydrodynamic parts *within* the optical scanning system. Individual particles are illuminated by laser sources, and fluorescence and elastic light scattering are collected by dedicated optics. The instrumental platform allows one to encircle the SFC with lasers and detectors, which provide an effective solution in analyzing individual particles. Automatic sampler, stepper-motor-controlled flow system, and a powerful electronic unit allow the effective control of the operation of the BioUniScan. The optical benches of the BioUniScan are flexible in operational wavelengths. The photograph of the BioUniScan system is shown in Figure 4.8.

The schematic layout of the BioUniScan optical system is presented in Figure 4.9. Two lasers are used to illuminate the particles within the cuvette. The coaxial laser 1 is used to generate the scattering pattern and the orthogonal laser 2 is used to excite the fluorescence, to control flow speed and as a reference point in time to angle transformation. The beam of laser 1 is directed coaxially with the stream by lens 1 through a hole in mirror 3. The hydrodynamic focusing head (flow cell in Figure 4.9) produces two concentric fluid streams: a sheath stream without particles and a probe stream that carries the analyzed particles. A differential

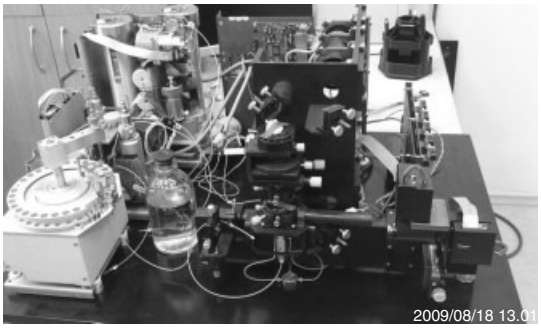

Figure 4.8 The instrumental platform of universal analyzer for biology and medicine "BioUniScan."

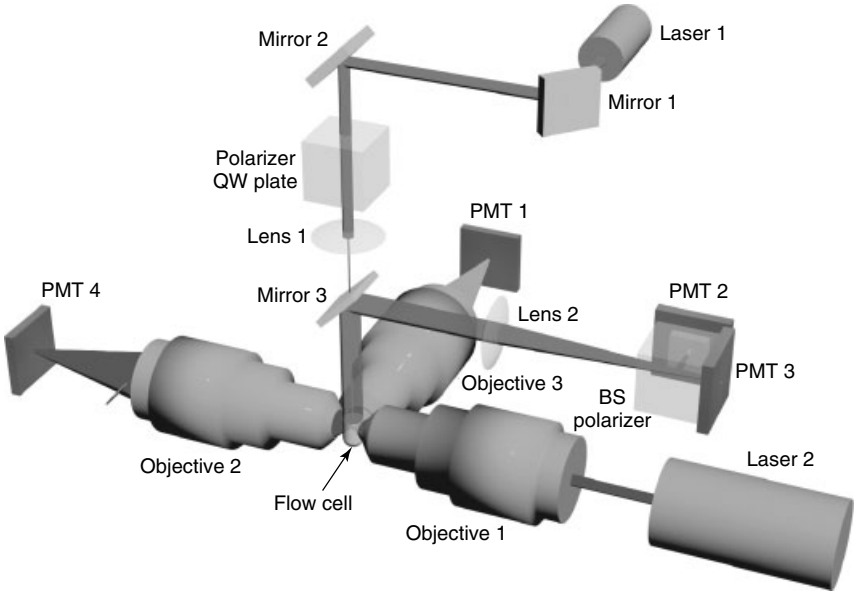

Figure 4.9 The schematic layout of the instrumental platform of universal analyzer for biology and medicine "BioUniScan."

pressure regulator is used for sample flow control. The fluidics system directs the streams into the capillary (diameter of 0.25 cm) of the flow cell (Figure 4.9). Finally fluidic system provides a probe stream with 12 μm diameter within the testing zone of the SFC. The hydrodynamically focused stream is fed into the cuvette at the spherical end through a cone where the hydrodynamic focusing head is connected by mechanical pressure. The flow channel is truncated in the flat end of the cuvette where it is connected to an orthogonal outlet. For this purpose, the cuvette is combined with a quartz plate. The 0.5 mm wide outlet is grooved at the flat end surface of the cuvette.

The LSP signal is obtained by measuring the signal intensity as a function of time by means of the light-scattering unit formed by mirror 3, lens 2, BS (beam splitter), polarizer, PMT 2, and PMT 3. Regular and polarized LSPs are measured by PMT 3 and PMT 2, respectively. The system is equipped with laser 2, which is orthogonal to the probe stream and provides the trigger signal by means of objective 2 and PMT 4. The latter, controlling the AD- converter, can also be taken from the fluorescence channel formed by objective 3 and PMT 1. In fact, the PMT 1 schematically represents the fluorescence unit of the BioUniScan formed by dichroic mirrors and band-pass filters requested. The ADC is operated continuously and the AD-conversion is interrupted for read out when a trigger signal is obtained.

4.4.1.2 **Mueller Matrix of the SFC**

The intensity and polarizing properties of a laser beam are described via a Stokes vector [48]. The transformation of the Stokes vector of incident light by interaction

with a particle within the optical system can be described by a corresponding Mueller matrix. Hence, the complete information on the scattering from a particle can be presented in the form of a 4 × 4 Mueller matrix [26]

$$M = \begin{pmatrix} S_{11} & S_{12} & S_{13} & S_{14} \\ S_{21} & S_{22} & S_{23} & S_{24} \\ S_{31} & S_{32} & S_{33} & S_{34} \\ S_{41} & S_{42} & S_{43} & S_{44} \end{pmatrix} \tag{4.14}$$

In general, the S_{ij} depends on polar θ and azimuthal ϕ scattering angles, $S_{ij} = S_{ij}(\theta, \phi)$. Averaging over ϕ from 0 to 360° by the SFC optical cuvette results in the following scattering intensity for circularly polarized incident laser beam:

$$I_r = \frac{1}{2\pi} \int_0^{2\pi} [S_{11}(\theta, \varphi) + S_{14}(\theta, \varphi)] \, d\varphi \tag{4.15}$$

$$I_p = \frac{1}{2\pi} \int_0^{2\pi} \big[S_{11}(\theta, \varphi) + S_{14}(\theta, \varphi) + (S_{21}(\theta, \varphi) + S_{24}(\theta, \varphi)) \cos(2\varphi) + (S_{31}(\theta, \varphi) + S_{34}(\theta, \varphi)) \sin(2\varphi) \big] \, d\varphi \tag{4.16}$$

for regular and polarized LSPs, respectively. For axisymmetric scatterers, Equation 4.15 becomes [49]

$$I(\theta) = \frac{1}{2\pi} \int_0^{2\pi} S_{11}(\theta, \varphi) d\varphi \tag{4.17}$$

4.4.2
Differential Scattering Cross Section of White Blood Cells

The essential feature of the SFC is the ability to measure the absolute DSCS of single particles of any shape and structure. This feature is realized by measurement of a mixture of unknown particles and polymer microspheres [13]. The LSP of the polymer microsphere, measured with the SFC, gives a high-accuracy agreement with Mie theory [45]. This allows calibration in absolute light-scattering units. The DSCS was calculated from the following equation:

$$\frac{d\sigma}{d\theta} = I_r(\theta) \left(\frac{\lambda}{2\pi m_0} \right)^2 \tag{4.18}$$

where I_r is the measured LSP (Equation 4.15), λ is the wavelength of the incident light, m_0 is the refractive index of the surrounding medium (1.337).

This method was applied to lymphocytes by Strokotov *et al.* [8] using $\lambda = 488$ nm. Fifty DSCSs of individual T lymphocytes and one polystyrene microsphere (diameter 1.8 μm) are presented in Figure 4.10. Variation in LSP structure and intensity among lymphocytes is discussed in Section 4.4.4. Orlova *et al.* [13] measured DCSC of neutrophils using $\lambda = 660$ nm. These results are presented in Figure 4.11, showing 25 LSPs of individual neutrophils and polystyrene microspheres (diameter 5 μm).

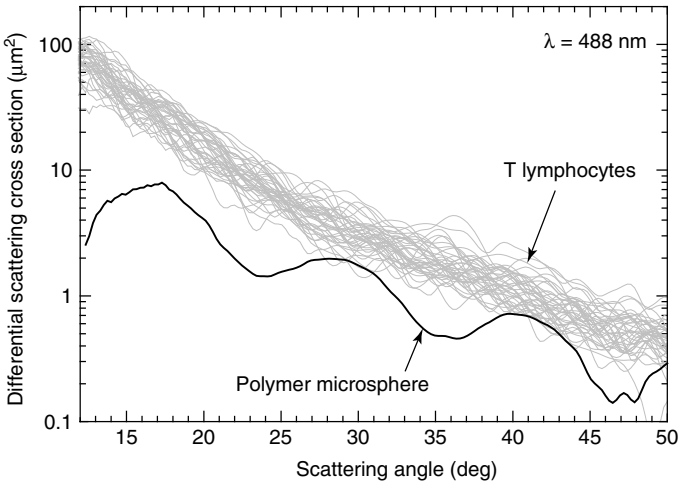

Figure 4.10 DSCS of T lymphocytes and a microsphere.

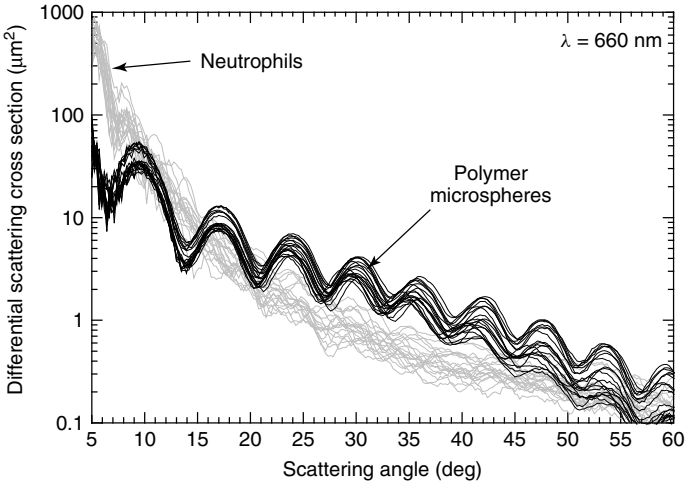

Figure 4.11 DSCS of neutrophils and polymer microspheres.

To directly compare lymphocytes and granulocytes, we have separated them from a single blood sample (Section 4.4.3) and measured their DSCS at the wavelength 488 nm. The results for representative number of individual cells as well as average of all lymphocytes and of all granulocytes in the sample are presented in Figure 4.12.

4.4.3 Measurement of Light Scattering of Mononuclear Cells

Ordinary flow cytometry allows one to measure the forward and side scattering from single cells, which can be used to discriminate lymphocytes, monocytes,

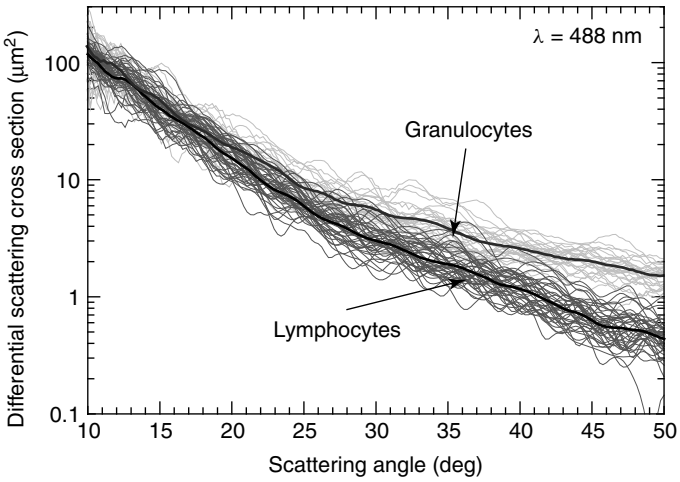

Figure 4.12 DSCS of lymphocytes and granulocytes. Bold lines are average DCSC over the whole sample for each cell type.

and granulocytes (Terstappen *et al.* [50]). Moreover, Terstappen *et al.* [51] reported the correlation between fraction of cells with large side scattering and fraction of cytotoxic lymphocytes, which can be potentially used to determine the latter fraction from light scattering only. Ding *et al.* [33] employed a goniometer system with a photoelastic modulation scheme to determine selected Mueller matrix elements of B cell hydrosol samples. The angular dependence of S_{11}, S_{12}, and S_{34} was determined from the scattered light signals between 10 and 160° at three wavelengths.

Angle-resolved light-scattering measurement of single mononuclear cells was pioneered by Doornbos *et al.* [52], who measured LSPs of optically trapped human lymphocytes in a range of scattering angles from 15 to 60°. Similar measurements for human monocyte in a full range of scattering angles were performed by Watson *et al.* [53]. LSPs of single cells were also measured by an SFC [6–8]. SFC can also be used in a two-parameter regime of ordinary flow cytometry to discriminate leukocytes subtypes [7]. Instead of side scattering, absolute values of the integrated whole light-scattering trace may be used. An example of such cytogram for a blood sample from a healthy donor is shown in Figure 4.13. Strokotov *et al.* [8] combined this discrimination with CD3 and CD19 immunofluorescence markers to identify T and B lymphocytes, respectively.

One possibility of looking at differences between T and B lymphocytes is by studying average LSPs. Averaged 100 experimental LSPs from the samples of T and B lymphocytes for a single donor are shown in Figure 4.14. There is difference in the intensity of scattering angles from 15 to 35°. However, this difference is much smaller than the natural variability of LSPs inside each sample (Figure 4.10). Strokotov *et al.* [8] showed that this difference can be partly explained

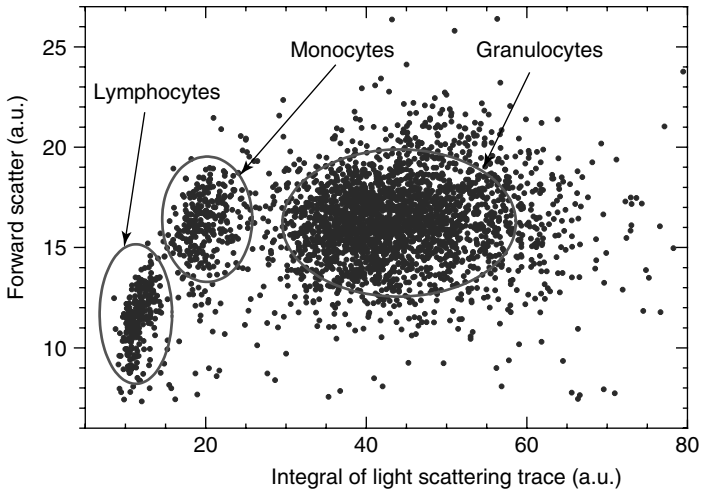

Figure 4.13 Light-scattering cytogram of leucocytes.

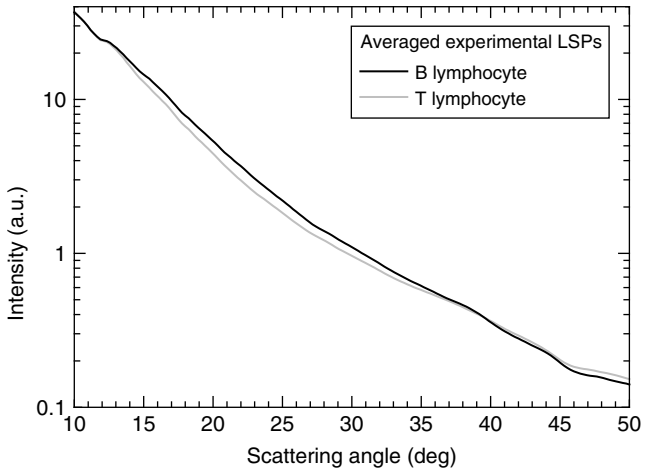

Figure 4.14 The experimental LSPs of T and B lymphocytes averaged over a sample.

by the difference in the mean diameter (Table 4.2); however, further study is required to clarify it.

4.4.4
Characterization of Mononuclear Cells from Light Scattering

Zharinov *et al.* [7] have analyzed a blood sample containing lymphocytes and monocytes using SFC and processed it with a five-layer spherical model. They have used multistart Levenberg–Marquardt algorithm (Section 4.3.3), which produced satisfactory results only for a small percentage of cells in a sample. The results

Table 4.2 Comparison of model characteristics of T and B lymphocytes of two donors.

	Donor 1		Donor 2	
	T	**B**	**T**	**B**
Sample size	225	146	330	86
$<D_c>$ (μm)	6.31	6.63	6.38	6.63
$\sigma(D_c)$(μm)	0.50	0.65	0.57	0.73
$\sigma(D_c)$(μm)	0.04	0.06	0.04	0.09
$<D_n/D_c>$	0.901	0.904	0.903	0.905
$\sigma(D_n/D_c)$	0.005	0.007	0.005	0.008
$\sigma(D_n/D_c)$	0.001	0.001	0.001	0.001
$<m_c>$	1.3759	1.3766	1.3765	1.3766
$\sigma(m_c)$	0.0026	0.0024	0.0026	0.0027
$\sigma(m_c)$	0.0005	0.0006	0.0004	0.0008
$<m_n>$	1.4479	1.4502	1.4476	1.4490
$\sigma(m_n)$	0.0080	0.0086	0.0080	0.0094
$\sigma(m_n)$	0.0007	0.0009	0.0006	0.0013

$<.>$, $\sigma(.)$, and $\sigma(<.>)$ denote estimated mean, standard deviation, and standard error of mean, respectively.

of this small fraction were used to characterize the whole sample. The following empirical correspondence between parameters of the five-layer model and studied cells was proposed: outer diameter of the third layer, that is the nucleus diameter; outer diameter of the fifth layer, that is, the cell diameter; refractive index of the fourth layer, that is, the cytoplasm refractive index; and the volumetric mean of refractive indices of first three layers, that is, the nucleus refractive index. Using this correspondence, it was shown that the obtained results fall within the range of literature data for lymphocytes and monocytes.

Strokotov *et al.* [8] measured leukocytes of seven donors identifying the T and B cells using the procedure described in Section 4.4.3. The global optimization algorithm described in Section 4.3.3 was applied to each cell. Results of this procedure for four typical cells from a sample of T cells of one donor are shown in Figure 4.15. Comparing this to Figure 4.7, one can see that the model errors for real lymphocytes are of the same magnitude as are the errors due to nuclear inhomogeneity with a volume fraction of only 10%. So, the latter may be responsible for a significant part of the former. However, more simulations are required to make any definite conclusions.

The characterization of the sample is performed as mentioned in Section 4.3.3.4. The ratio of LSPs that passed the confidence level threshold varied from 10% to 20% from sample to sample. On the basis of simulations described in Section 4.3.3.3, Strokotov *et al.* [8] suggested that using the threshold $\alpha_0 = 0.8$ leaves only cells with a relatively homogeneous nucleus (but possibly shifted from the center of the cell). These may be the cells that are in the G1-phase of a cell cycle [54].

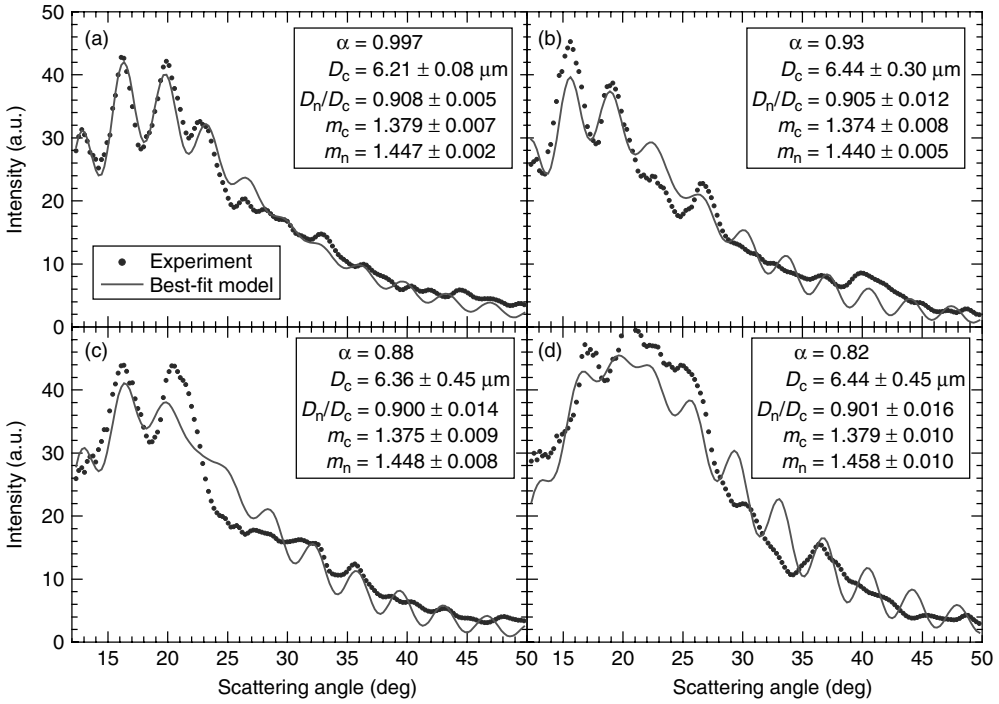

Figure 4.15 Results of global optimization for four experimental LSPs of T lymphocytes showing experimental and best-fit weighted LSPs. The graphs correspond to different reliability level of the fit α, decreasing from (a) to (d). Estimates of the cell characteristics (expectation value ± standard deviation) are also shown.

Unfortunately, the number of processed B lymphocytes that passed the threshold was statistically small for most of the samples except two. Results for the latter comparing B and T lymphocytes are shown in Table 4.2.

Analyzing literature data on cell and nucleus diameters obtained by the Coulter principle and electron and optical microscopy, Strokotov *et al.* [8] concluded that there is a disagreement between different methods, but current results fall within the broad range of existing data. However, there is an unusually small variation in the mean size of T cells and their nucleii among all seven donors (even accounting for error of mean). This fact disagrees with recent microscopic measurements [10, 17], which currently cannot be explained. A detailed study combining SFC-based and microscopic methods is required to resolve this issue.

Comparing the results of the global optimization for characterization of T and B lymphocytes (Table 4.2), one can see that the main difference in T and B cell morphology is the mean cell size, $<D_c>$. Although the difference in $<D_c>$ of about 5% is statistically significant, it is smaller than the estimated biological variability $\sigma(D_c)$ in each sample. Hence, at present, one cannot reliably classify a single

lymphocyte as being T- or B-, using only its morphological characteristics that are determined from LSP. However, it may be possible to estimate the relative count of T to B lymphocytes in a sample, processing the distribution of all lymphocytes over morphological characteristics as a bimodal distribution (similar to Terstappen *et al.* [51]).

Strokotov *et al.* [8] also noted that B cells are generally better fitted by the coated sphere model than T cells, which may be caused by smaller deviation in the shape of B lymphocytes from the coated sphere; in particular, by a relatively smaller inhomogeneity of the nucleus.

4.4.5
Measurement of Light Scattering of Granular Cells

Light scattering from a suspension of granulocytes was employed in dynamical studies. Light-scattering intensity was used as a measure of neutrophil aggregation [55] and change in shape [56]. Neutrophil degranulation was shown to correlate with right-angle light-scattering intensity [57] and granulocyte aggregation – with light extinction [58]. Flow cytometrical studies of neutrophil biology were reviewed by Carulli [59].

In flow cytometers, granulocytes can be discriminated from other leukocytes by their higher forward and side scattering, except the basophils which are found in the light-scattering region of lymphocytes [60]. To perform further discrimination of granulocytes in order to classify them into subclasses, more measured parameters are needed. This can be achieved by using monoclonal antibodies to particular surface antigens or by measuring autofluorescence (reviewed by Semyanov *et al.* [6]). Depolarized side scattering, a parameter proposed by de Grooth *et al.* [35], can be used to discriminate eosinophils from neutrophils. This was actually employed in cytometrical protocol, applying higher value of this signal for eosinophils [50, 61]. Only recently, Yurkin *et al.* [12] showed that this experimental fact can be explained by the difference in granule sizes of neutrophils and eosinophils (Section 4.3.2.1).

LSPs of individual granulocytes were measured using an optical trap [53] and an SFC [6]. However, it was not specifically determined to which subtype of granulocytes the analyzed cells belonged.

Orlova *et al.* [13] used an SFC to measure LSPs of neutrophils that were identified using CD16b fluorescent markers. Samples from four donors were studied. Twenty-five randomly chosen experimental LSPs from the first sample are shown in Figure 4.16 together with the most similar LSP from theoretical DDA simulation. The simulation was performed for an optical model of the neutrophil (Figure 4.3b) with the following parameters: cell size of 9.6 μm, granule diameter of 0.2 μm with a volume fraction of 0.1, and nucleus volume fraction of 0.1. Experimental LSPs demonstrate a relatively large variability in their intensities and shapes, and theoretical LSP falls within the range of this variation, supporting the adequacy of the optical model. However, Orlova *et al.* [13] noted that simulated LSPs do not agree with experimental LSPs of other three samples as well, as they do with the first one. So, further theoretical study by varying the model parameters is required.

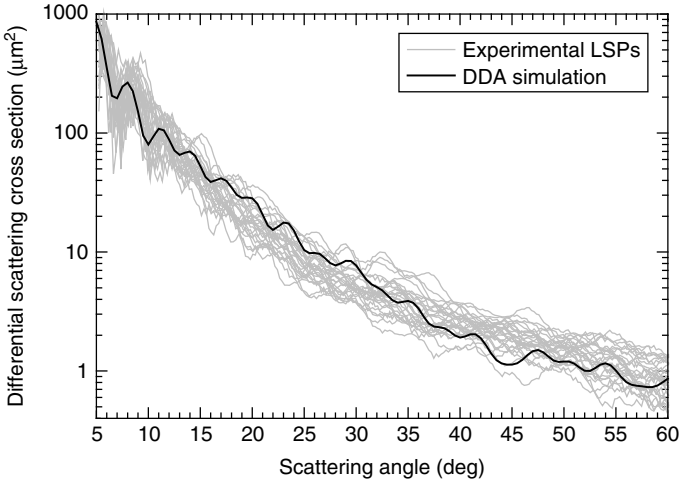

Figure 4.16 The experimental LSPs of single neutrophils (gray) and LSP calculated by DDA (black) from the optical model of the cell.

To illustrate the difference between LSPs of neutrophils from four donors, Figure 4.17 presents LSPs averaged over all neutrophils in each sample. These averaged LSPs are almost featureless except for a minimum and maximum between 7 and 10°. These extrema are present in all individual LSPs (Figure 4.16) as well as in the averaged LSP. The position of extrema in individual LSPs for small scattering angles is mostly determined by neutrophil diameter; that is, it can be described by diffraction. The simulated LSPs also have these two extrema at similar angles, which proves that more or less correct size was used for the neutrophil model.

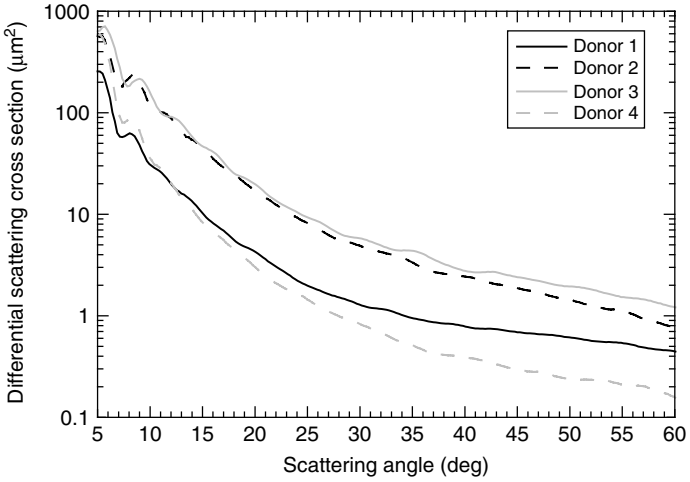

Figure 4.17 The experimental LSPs of neutrophils of four donors averaged over sample.

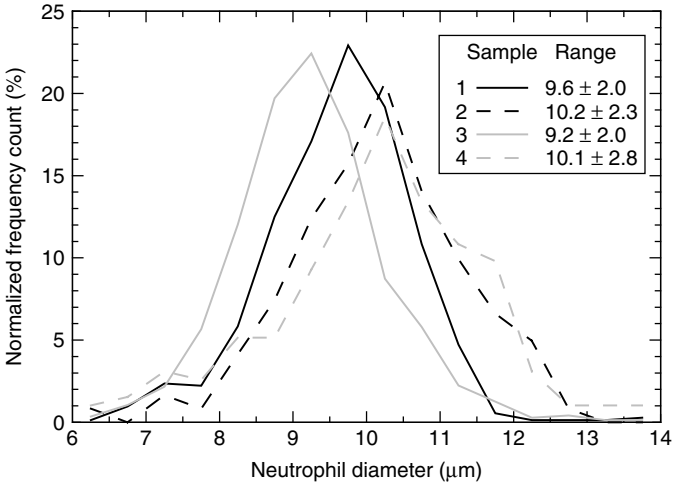

Figure 4.18 Size distributions of neutrophils from four samples determined by the spectral method.

The complete characterization of granulocytes, and neutrophils in particular, does not seem currently possible due to their complexity, as compared to the characterization of mononuclear cells (Section 4.4.4). That is why Orlova *et al.* [13] proposed to use averaged LSPs as a diagnostic parameter because these are essentially different between individuals; for example, they have different overall magnitudes and decay rates for larger scattering angles. These differences are caused by morphological differences in neutrophils; however, clinical study of both normal and abnormal samples is required to clarify the diagnostic value of the averaged LSP.

Experimental LSPs were also processed with a spectral sizing method (Section 4.3.3), although applicability of the latter for granulocytes has not been thoroughly studied. Size distributions of neutrophils from four samples are shown in Figure 4.18. On the basis of comparison with a recent microscopic study [17], Orlova *et al.* [13] concluded that spectral sizing method produces meaningful results for neutrophils (mean values within normal physiological ranges), but results for each individual cell may contain significant random errors leading to widening of distributions. Moreover, the difference in sample-averaged neutrophil sizes between the samples is less than 10%. This implies that significant changes in neutrophil internal structure (granularity, nucleus size, refractive indices, etc.) must be considered to explain the fivefold intersample variation of LSP magnitude (Figure 4.17).

4.5 Conclusion

In this chapter, we have summarized the state of the art of light-scattering studies of WBCs. The ultimate goal of these studies is to reliably measure light-scattering

signals and use them to deduce morphological characteristics of the cells. The latter relies on a solution of inverse light-scattering problem based on an adequate optical model of a WBC. The complexity of this goal lies in the combination of different experimental and theoretical techniques; to name a few: confocal microscopy, DDA, SFC, and global optimization.

Recent progress in related techniques as well as a smart combination of them has led to a significant progress in the field of light scattering by WBCs. In particular, this chapter describes recent results for lymphocytes and neutrophils, obtained using SFC. A method to obtain detailed morphological characterization from the measured light-scattering pattern was developed for lymphocytes (as well as for other mononuclear cells), which allowed determination of size and refractive index of both the cell and the nucleus of individual cells. For neutrophils, a good agreement between experiments and theoretical simulations was obtained, which supports the overall adequacy of the proposed optical model.

New knowledge about optical properties of the WBCs should encourage researchers to develop new methods for enhanced characterization of blood cells with optical technologies, and to incorporate these methods into automatic cell analyzers. New cellular characteristics should provide medical doctors with additional indicators, which could play an important role in the analysis of abnormal cellular phenomenon, of patient pathologies.

Acknowledgments

We thank our current and former colleagues from the Laboratory of Cytometry and Biokinetics: Andrey Chernyshev, Konstantin Gilev, Vyacheslav Nekrasov, Konstantin Semyanov, and Dmitry Strokotov.

We also acknowledge the financial support from Siberian Branch of the Russian Academy of Sciences (integration grant N7-2009), the Presidium of the Russian Academy of Sciences (grant N4.5.10), the President of the Russian Federation programme for state support of the leading scientific schools (grant number: NSh-65387.2010.4.) and program of the Russian Government ''Research and educational personnel of innovative Russia'' (contracts P422, P2497, and P1039).

References

1. Greer, J.P., Foerster, J., and Lukens, J.N. (eds) (2003) *Wintrobe's Clinical Hematology*, 11th edn, Lippincott Williams & Wilkins Publishers, Baltimore.
2. Maltsev, V.P. and Semyanov, K.A. (2004) *Characterisation of Bio-Particles from Light Scattering*, VSP, Utrecht.
3. Brock, R.S., Hu, X., Weidner, D.A., Mourant, J.R., and Lu, J.Q. (2006) Effect of detailed cell structure on light scattering distribution: FDTD study of a B-cell with 3D structure constructed from confocal images. *J. Quant. Spectrosc. Radiat. Transfer*, **102**, 25–36.
4. Neukammer, J., Gohlke, C., Höpe, A., Wessel, T., and Rinneberg, H. (2003) Angular distribution of light scattered by single biological cells and oriented

particle agglomerates. *Appl. Opt.*, **42**, 6388–6397.
5. Yang, Y., Zhang, Z., Yang, X., Yeo, J.H., Jiang, L., and Jiang, D. (2004) Blood cell counting and classification by non-flowing laser light scattering method. *J. Biomed. Opt.*, **9**, 995–1001.
6. Semyanov, K.A., Zharinov, A.E., Tarasov, P.A., Yurkin, M.A., Skribunov, I.G., and van Bockstaele, D.R. *et al.* (2007) in *Optics of Biological Particles* (eds A.G. Hoekstra, V.P. Maltsev, and G. Videen), Springer, Dordrecht, pp. 269–280.
7. Zharinov, A.E., Tarasov, P.A., Shvalov, A.N., Semyanov, K.A., van Bockstaele, D.R., and Maltsev, V.P. (2006) A study of light scattering of mononuclear blood cells with scanning flow cytometry. *J. Quant. Spectrosc. Radiat. Transfer*, **102**, 121–128.
8. Strokotov, D.I., Yurkin, M.A., Gilev, K.V., van Bockstaele, D.R., Hoekstra, A.G., Rubtsov, N.B., and Maltsev, V.P. (2009) Is there a difference between T- and B- lymphocyte morphology? *J. Biomed. Opt.*, **14**, 064036–064012.
9. Hoekstra, A.G., Grimminck, M.D., and Sloot, P.M.A. (1998) Large scale simulation of elastic light scattering by a fast discrete dipole approximation. *Int. J. Mod. Phys. C*, **9**, 87–102.
10. Loiko, V.A., Ruban, G.I., Gritsai, O.A., Gruzdev, A.D., Kosmacheva, S.M., Goncharova, N.V., and Miskevich, A.A. (2006) Morphometric model of lymphocyte as applied to scanning flow cytometry. *J. Quant. Spectrosc. Radiat. Transfer*, **102**, 73–84.
11. Dunn, A.K. (2007) in *Optics of Biological Particles* (eds A.G. Hoekstra, V.P. Maltsev, and G. Videen.), Springer, Dordrecht, pp. 19–29.
12. Yurkin, M.A., Semyanov, K.A., Maltsev, V.P., and Hoekstra, A.G. (2007) Discrimination of granulocyte subtypes from light scattering: theoretical analysis using a granulated sphere model. *Opt. Express*, **15**, 16561–16580.
13. Orlova, D.Y., Yurkin, M.A., Hoekstra, A.G., and Maltsev, V.P. (2008) Light scattering by neutrophils: model, simulation, and experiment. *J. Biomed. Opt.*, **13**, 054057–054057.
14. Livesey, S.A., Buescher, E.S., Krannig, G.L., Harrison, D.S., Linner, J.G., and Chiovetti, R. (1989) Human neutrophil granule heterogeneity: immunolocalization studies using cryofixed, dried and embedded specimens. *Scanning Microsc. Suppl.*, **3**, 231–239.
15. Bainton, D.F. (1993) Neutrophilic leukocyte granules: from structure to function. *Adv. Exp. Med. Biol.*, **336**, 17–33.
16. Bjerrum, O.W. (1993) Human neutrophil structure and function with special reference to cytochrome b559 and beta 2-microglobulin. *Dan. Med. Bull.*, **40**, 163–189.
17. Ruban, G.I., Kosmacheva, S.M., Goncharova, N.V., Van Bockstaele, D., and Loiko, V.A. (2007) Investigation of morphometric parameters for granulocytes and lymphocytes as applied to a solution of direct and inverse light-scattering problems. *J. Biomed. Opt.*, **12**, 044017.
18. Brederoo, P., van der Meulen, J., and Mommaas-Kienhuis, A.M. (1983) Development of the granule population in neutrophil granulocytes from human bone marrow. *Cell Tiss. Res.*, **234**, 469–496.
19. Brunsting, A. and Mullaney, P.F. (1974) Differential light scattering from spherical mammalian cells. *Biophys. J.*, **14**, 439–453.
20. Metcalf, W.K., Metcalf, N.F., and Gould, R.N. (1978) Lymphocyte cytoplasmic refractive index (LCRI). *Antibiot. Chemother.*, **22**, 149–154.
21. Mourant, J.R., Canpolat, M., Brocker, C., Esponda-Ramos, O., Johnson, T.M., Matanock, A. *et al.* (2000) Light scattering from cells: the contribution of the nucleus and the effects of proliferative status. *J. Biomed. Opt.*, **5**, 131–137.
22. Barer, R. and Joseph, S. (1954) Refractometry of living cells: Part I. Basic principles. *Quart. J. Microsc. Sci.*, **95**, 399–423.
23. Dunn, A. and Richards-Kortum, R. (1996) Three-dimensional computation of light scattering from cells. *IEEE J. Select. Topics Quant. Electr.*, **2**, 898–905.
24. Dunn, A., Smithpeter, C., Welch, A.J., and Richards-Kortum, R. (1997)

Finite-difference time-domain simulation of light scattering from single cells. *J. Biomed. Opt.*, **2**, 262–266.
25. Chaumet, P.C. and Belkebir, K. (2009) Three-dimensional reconstruction from real data using a conjugate gradient-coupled dipole method. *Inv. Probl.*, **25**, 024003.
26. Bohren, C.F. and Huffman, D.R. (1983) *Absorption and Scattering of Light by Small Particles*, John Wiley & Sons, Inc., New York.
27. Yang, W. (2003) Improved recursive algorithm for light scattering by a multilayered sphere. *Appl. Opt.*, **42**, 1710–1720.
28. Mishchenko, M.I., Travis, L.D., and Lacis, A.A. (2002) *Scattering, Absorption, and Emission of Light by Small Particles*, Cambridge University Press, Cambridge.
29. Doicu, A., Wriedt, T., and Eremin, Y.A. (2006) *Light Scattering by Systems of Particles: Null-field Method with Discrete Sources: Theory and Programs*, Springer, Berlin.
30. Yurkin, M.A. and Hoekstra, A.G. (2007) The discrete dipole approximation: an overview and recent developments. *J. Quant. Spectrosc. Radiat. Transfer*, **106**, 558–589.
31. Taflove, A. and Hagness, S.C. (2005) *Advances in Computational Electrodynamics: The Finite-Difference Time-Domain Method*, 3rd edn, Artech House, Boston.
32. Ngo, D., Videen, G., and Chýlek, P. (1996) A FORTRAN code for the scattering of EM waves by a sphere with a nonconcentric spherical inclusion. *Comput. Phys. Commun.*, **99**, 94–112.
33. Ding, H., Lu, J.Q., Brock, R.S., McConnell, T.J., Ojeda, J.F., Jacobs, K.M., and Hu, X.H. (2007) Angle-resolved Mueller matrix study of light scattering by R-cells at three wavelengths of 442, 633, and 850 nm. *J. Biomed. Opt.*, **12**, 034032.
34. Yurkin, M.A., Hoekstra, A.G., Brock, R.S., and Lu, J.Q. (2007) Systematic comparison of the discrete dipole approximation and the finite difference time domain method for large dielectric scatterers. *Opt. Express*, **15**, 17902–17911.
35. de Grooth, B.G., Terstappen, L.W.M.M., Puppels, G.J., and Greve, J. (1987) Light-scattering polarization measurements as a new parameter in flow cytometry. *Cytometry*, **8**, 539–544.
36. Yurkin, M.A., Maltsev, V.P., and Hoekstra, A.G. (2007) The discrete dipole approximation for simulation of light scattering by particles much larger than the wavelength. *J. Quant. Spectrosc. Radiat. Transfer*, **106**, 546–557.
37. Semyanov, K.A., Tarasov, P.A., Zharinov, A.E., Chernyshev, A.V., Hoekstra, A.G., and Maltsev, V.P. (2004) Single-particle sizing from light scattering by spectral decomposition. *Appl. Opt.*, **43**, 5110–5115.
38. Yurkin, M.A. (2007) Discrete dipole simulations of light scattering by blood cells. PhD thesis. University of Amsterdam.
39. Jones, D.R., Perttunen, C.D., and Stuckman, B.E. (1993) Lipschitzian optimization without the Lipschitz constant. *J. Optim. Theor. Appl.*, **79**, 157–181.
40. Seber, G.A.F. and Wild, C.J. (2003) *Nonlinear Regression*, Wiley-Interscience, Hoboken, NJ.
41. Bates, D.M. and Watts, D.G. (1988) *Nonlinear Regression Analysis and its Applications*, John Wiley & Sons, Inc., New York.
42. Fuller, W.A. (1990) in *Statistical Analysis of Measurement Error Models and Applications* (eds P.J. Brown and W.A. Fuller), American Mathematical Society, Providence, Rhode Island, pp. 41–58.
43. Maltsev, V.P., Chernyshev, A.V., Semyanov, K.A., and Soini, E. (1996) Absolute real-time measurement of particle size distribution with the flying light-scattering indicatrix method. *Appl. Opt.*, **35**, 3275–3280.
44. Maltsev, V.P. and Lopatin, V.N. (1997) A parametric solution of the inverse light-scattering problem for individual spherical particles. *Appl. Opt.*, **36**, 6102–6108.
45. Soini, J.T., Chernyshev, A.V., Hanninen, P.E., Soini, E., and Maltsev, V.P. (1998) A new design of the flow cuvette and optical set-up for the scanning flow cytometer. *Cytometry*, **31**, 78–84.

46. Maltsev, V.P. (2000) Scanning flow cytometry for individual particle analysis. *Rev. Sci. Instrum.*, **71**, 243–255.

47. Maltsev, V.P. and Chernyshev, A.V. (1997) US Patent Number 5,650,847. Date of patent: July 22, 1997.

48. Collett, E. (1993) *Polarized Light: Fundamentals and Applications*, Marcel Dekker, New York.

49. Yurkin, M.A., Semyanov, K.A., Tarasov, P.A., Chernyshev, A.V., Hoekstra, A.G., and Maltsev, V.P. (2005) Experimental and theoretical study of light scattering by individual mature red blood cells by use of scanning flow cytometry and a discrete dipole approximation. *Appl. Opt.*, **44**, 5249–5256.

50. Terstappen, L.W.M.M., de Grooth, B.G., Visscher, K., van Kouterik, F.A., and Greve, J. (1988) Four-parameter white blood cell differential counting based on light scattering measurements. *Cytometry*, **9**, 39–43.

51. Terstappen, L.W., De Grooth, B.G., Ten Napel, C.H., Van Berkel, W., and Greve, J. (1986) Discrimination of human cytotoxic lymphocytes from regulatory and B-lymphocytes by orthogonal light scattering. *J. Immunol. Methods*, **95**, 211–216.

52. Doornbos, R.M.P., Schaeffer, M., Hoekstra, A.G., Sloot, P.M.A., de Grooth, B.G., and Greve, J. (1996) Elastic light-scattering measurements of single biological cells in an optical trap. *Appl. Opt.*, **35**, 729–734.

53. Watson, D., Hagen, N., Diver, J., Marchand, P., and Chachisvilis, M. (2004) Elastic light scattering from single cells: orientational dynamics in optical trap. *Biophys. J.*, **87**, 1298–1306.

54. Murray, A. and Hunt, T. (1993) *The Cell Cycle*, Oxford University Press, Oxford.

55. Niwa, M., Kanamori, Y., Kohno, K., Matsuno, H., Kozawa, O., and Kanamura, M. *et al.* (2000) Usefulness of grading of neutrophil aggregate size by laser-light scattering technique for characterizing stimulatory and inhibitory effects of agents on aggregation. *Life Sci.*, **67**, 1525–1534.

56. Ehrengruber, M.U., Deranleau, D.A., and Coates, T.D. (1996) Shape oscillations of human neutrophil leukocytes: characterization and relationship to cell motility. *J. Exp. Biol.*, **199**, 741–747.

57. Sklar, L.A., Oades, Z.G., and Finney, D.A. (1984) Neutrophil degranulation detected by right angle light scattering: spectroscopic methods suitable for simultaneous analyses of degranulation or shape change, elastase release, and cell aggregation. *J. Immunol.*, **133**, 1483–1487.

58. Yuli, I. and Snyderman, R. (1984) Light scattering by polymorphonuclear leukocytes stimulated to aggregate under various pharmacologic conditions. *Blood*, **64**, 649–655.

59. Carulli, G. (1996) Applications of flow cytometry in the study of human neutrophil biology and pathology. *Haemapathol. Mol. Hematol.*, **10**, 39–61.

60. Terstappen, L.W.M.M., Johnson, D., Mickaels, R.A., Chen, J., Olds, G., Hawkins, J.T., Loken, M.R., and Levin, J. (1991) Multidimensional flow cytometric blood cell differentiation without erythrocyte lysis. *Blood Cells*, **17**, 585–602.

61. Lavigne, S., Bosse, M., Boulet, L.P., and Laviolette, M. (1997) Identification and analysis of eosinophils by flow cytometry using the depolarized side scatter-saponin method. *Cytometry*, **29**, 197–203.